

Structure and physical properties of new layered iron oxychalcogenide $\text{BaFe}_2\text{OSe}_2$

Hechang Lei,¹ Hyejin Ryu,^{1,2} John Warren,³ A. I. Frenkel,⁴ V. Ivanovski,⁵ B. Cekic⁵ and C. Petrovic^{1,2}

¹*Condensed Matter Physics and Materials Science Department,
Brookhaven National Laboratory, Upton, New York 11973, USA*

²*Department of Physics and Astronomy, Stony Brook University, Stony Brook, New York 11794-3800, USA*

³*Instrumentation Division, Brookhaven National Laboratory, Upton, New York 11973, USA*

⁴*Physics Department, Yeshiva University, 245 Lexington Avenue, New York, New York 10016, USA*

⁵*Institute of Nuclear Sciences Vinca, University of Belgrade, Belgrade 11001, Serbia*

(Dated: March 8, 2013)

We have successfully synthesized a new layered iron oxychalcogenide $\text{BaFe}_2\text{OSe}_2$ single crystal. This compound is built up of Ba and Fe-Se(O) layers alternatively stacked along the c-axis. The Fe-Se(O) layers contain double chains of edge-shared Fe-Se(O) tetrahedra that propagate along the b-axis and are bridged by oxygen along the a-axis. Physical property measurements indicate that $\text{BaFe}_2\text{OSe}_2$ is a semiconductor without the Curie-Weiss behavior up to 350 K. There is a possible long range antiferromagnetic (AFM) transition at 240 K, corresponding to the peak in specific heat measurement and two glassy transitions at 115 K and 43 K. The magnetic entropy up to 300 K is much smaller than the expected value for Fe^{2+} in tetrahedral crystal fields and Mössbauer spectrum indicates that long range magnetic order is unlikely at 294 K. Both results suggest that a short range magnetic correlations exist above the room temperature.

PACS numbers: 75.50.Ee, 75.10.Pq, 75.30.Gw, 75.47.Np

I. INTRODUCTION

The discovery of layered iron oxypnictides ($\text{Ln}(\text{O},\text{F})\text{FeAs}$, Ln = rare earth elements, 1111-type) superconductors with T_c up to 56 K,¹ has stimulated great interest in mixed-anion materials. Mixed anions from the same row of the Mendeleev periodic table tend to randomly occupy the same crystallographic site (anion disorder) because of the relatively similar sizes. On the other hand, if the anions are from different rows (oxysulfide or oxyselenide compounds for example), the distinctive difference of anion sizes and ionic polarization might lead to ordered occupancy in the different crystallographic sites (anion order), often forming layered crystal structure.²

The mixed-anion compounds have attracted some interest during the exploration of novel cuprate high temperature superconductors. Halooxocuprates are example where copper ions are coordinated with four oxygen ions, forming the CuO_2 sheet, whereas the halogen ion usually occupies a so-called apical site.³ With proper electron or hole doping, halooxocuprates will become superconductors.³ Besides superconductivity, mixed-anion materials also exhibit diverse physical properties. Copper oxychalcogenides LnCuOCh (Ch = S, Se, and Te), isostructural to 1111-type iron-based superconductors, are wide-gap p-type semiconductors with transparent p-type conductivity, photoluminescence, and large third order optical nonlinearity.^{4–6} Transition metal oxychalcogenides $\text{Ln}_2\text{O}_2\text{TM}_2\text{OCh}_2$ (TM = Mn, Fe, and Co) contain the layers built up by the edge-shared octahedral unit $[\text{TM}_2\text{OCh}_2]^{2-}$. These materials show strong electron-electron interactions (Mott insulators) on the two dimensional (2D) frustrated antiferromagnetic (AFM) checkerboard spin-lattice.^{7–9}

The materials with $[\text{TM}_2\text{OCh}_2]^{2-}$ layers exhibit similar structural diversity to iron-based superconductors. This is understandable since new compounds can be obtained by simply replacing $[\text{FeAs}]^-$ layers with $[\text{TM}_2\text{OCh}_2]^{2-}$ layers, such as $\text{LnOFeAs} \rightarrow \text{Ln}_2\text{O}_2\text{TM}_2\text{OCh}_2$, AEFFeAs (AE = alkali earth metals) $\rightarrow \text{AE}_2\text{F}_2\text{TM}_2\text{OCh}_2$,^{10–12} and AFeAs (A = alkali metals) $\rightarrow \text{Na}_2\text{Fe}_2\text{OSe}_2$.^{13–15} Thus, it is of considerable interest to explore the structural derivatives of AEFe_2As_2 among the oxychalcogenide compounds.

Here, we report the detailed synthesis and physical properties of a new layered iron oxychalcogenide $\text{BaFe}_2\text{OSe}_2$ single crystal. Even though it has the same chemical formula and $[\text{TM}_2\text{OCh}_2]^{2-}$ layers, the structure is different from other iron oxychalcogenides with $[\text{TM}_2\text{OCh}_2]^{2-}$ layers. To the best of our knowledge, $\text{BaFe}_2\text{OSe}_2$ is the first layered iron oxychalcogenide with alkali earth metal. It shows a semiconducting behavior with possible successive spin-glass transitions at low temperature and short range antiferromagnetic order above the room temperature.

II. EXPERIMENT

Single crystals of $\text{BaFe}_2\text{OSe}_2$ were synthesized by a self-flux method. Ba rod, Fe powder, Fe_2O_3 powder and Se shot were used as starting materials. BaSe was pre-reacted by reacting Ba piece with Se shot at 800 °C for 12 hours. BaSe was mixed with other reagents and intimately ground together using an agate pestle and mortar. The ground powder was pressed into pellets, loaded in an alumina crucible and then sealed in quartz tubes with Ar under the pressure of 0.2 atmosphere. The quartz tubes were heated up to 600 °C in 10 h, kept at 600 °C for 12 h, ramped again to 1100 °C in 12 h, kept at 1100 °C for

12 h, and then cooled slowly at a rate of 3 °C/h to 800 °C, finally the furnace was shut down and the sample was cooled down to room temperature naturally. Black plate-like crystals with typical size $2 \times 2 \times 0.5 \text{ mm}^3$ can be grown. Except for heat-treatment, all of processes for sample preparation were performed in glove boxes filled with argon.

The crystal structure of $\text{BaFe}_2\text{OSe}_2$ crystal was identified by single crystal x-ray diffraction (XRD). The data were collected using the Bruker APEX2 software package¹⁶ on a Bruker SMART APEX II single crystal x-ray diffractometer with graphite-monochromated Mo K_α radiation ($\lambda = 0.71073 \text{ \AA}$) at room temperature. Data processing and an empirical absorption correction were also applied using APEX2 software package. The structures were solved (direct methods) and refined by full-matrix least-squares procedures on $|F^2|$ using Bruker SHELXTL program software.¹⁷ Obtained lattice parameters of $\text{BaFe}_2\text{OSe}_2$ are given in Table 1. Atomic coordinates, isotropic displacement parameters and selected interatomic bond distances and angles are listed in Table 2. Phase identity and purity were confirmed by powder X-ray diffraction carried out on a Rigaku miniflex X-ray machine with Cu K_α radiation ($\lambda = 1.5418 \text{ \AA}$). Structural refinements of powder $\text{BaFe}_2\text{OSe}_2$ sample was carried out by using Rietica software.¹⁸

The average stoichiometry was determined by examination of multiple points using an energy-dispersive X-ray spectroscopy (EDX) in a JEOL JSM-6500 scanning electron microscope. The presence of oxygen was confirmed for $\text{BaFe}_2\text{OSe}_2$, but the exact amount could not be quantified because of experimental limitations. The average atomic ratios determined from EDX are Ba:Fe:Se = 1.00(7):2.2(2):2.0(2), close to the ratio of stoichiometric $\text{BaFe}_2\text{OSe}_2$.

Mössbauer spectrum was taken in transmission mode with $^{57}\text{Co(Rh)}$ source at 294 K and the parameters were obtained using WinNormos software.²⁰ Calibration of the spectrum was performed by laser and isomer shifts were given with respect to $\alpha\text{-Fe}$.

The X-ray absorption spectra of the Fe and Se K -edges were taken in transmission mode on powder samples of $\text{BaFe}_2\text{OSe}_3$ at the X19A beamline of the National Synchrotron Light Source. Standard procedure was used to extract the extended x-ray absorption fine-structure (EXAFS) from the absorption spectrum.¹⁹

Electrical transport, heat capacity, and magnetization measurements were carried out in Quantum Design PPMS-9 and MPMS-XL5.

III. RESULTS AND DISCUSSION

Similar to $\text{K}_x\text{Fe}_{2-y}\text{Se}_2$ and BaFe_2Se_3 ,^{21,22} the structure of $\text{BaFe}_2\text{OSe}_2$ is built up by stacking the Ba cations and Fe-Se(O) layers alternatively along the c axis (Fig. 1(a)). However, within the Fe-Se(O) layers, the connection of Fe-Se(O) tetrahedra in $\text{BaFe}_2\text{OSe}_2$ is distinctive

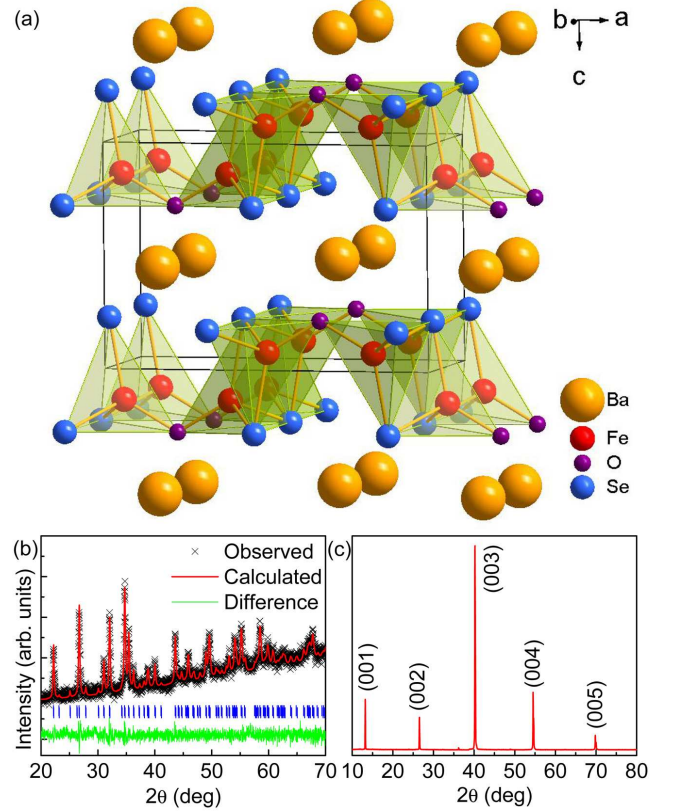


FIG. 1. (a) Crystal structure of $\text{BaFe}_2\text{OSe}_2$. The biggest orange, big red, medium blue and small purple balls represent Ba, Fe, O and Se ions, respectively. (b) and (c) Powder and single crystal XRD patterns of $\text{BaFe}_2\text{OSe}_2$.

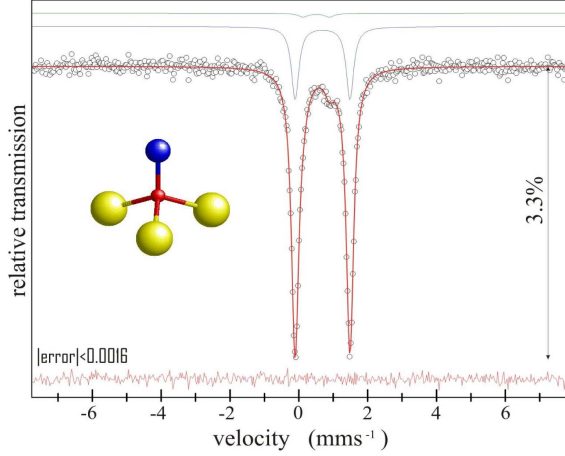
different from those in $\text{K}_x\text{Fe}_{2-y}\text{Se}_2$ and BaFe_2Se_3 . In $\text{BaFe}_2\text{OSe}_2$, double chains of edge-shared Fe-Se(O) tetrahedra propagate along the Se atoms parallel to b -axis. The Fe-Se(O) double chains are bridged by oxygen along the a -axis (Fig. 1(a)). The bond distances of Fe-Se ($\sim 2.5 \text{ \AA}$) and Fe-O ($\sim 1.9 \text{ \AA}$) are very similar to distances in compounds where Fe is also in tetrahedral coordination (BaFe_2Se_3 : $d_{\text{Fe-Se}} \sim 2.4 \text{ \AA}$, Fe_3O_4 : $d_{\text{Fe-O}} \sim 1.9 \text{ \AA}$). Because of different bond distances between Fe-Se and Fe-O, Fe atoms are located at the highly distorted tetrahedral environment when compared to other materials with pure Fe-Se tetrahedra. This distortion is also reflected in the significant deviation of bond angles from the value for the ideal tetrahedron (109.5°). The bond angles range up to $130.38(10)^\circ$ in $\text{BaFe}_2\text{OSe}_2$, much larger than the values in BaFe_2Se_3 and $\text{K}_x\text{Fe}_{2-y}\text{Se}_2$.^{22,23} Moreover, the different connection of Fe-Se(O) leads to the larger nearest neighbor Fe-Fe distances ($d_{\text{Fe-Fe}}$ ($\sim 3.13 \text{ \AA}$)) when compared to BaFe_2Se_3 and $\text{K}_x\text{Fe}_{2-y}\text{Se}_2$.^{22,23} Using obtained Fe-Se and Fe-O bond lengths as shown in Table 2, the valence of Fe ions in $\text{BaFe}_2\text{OSe}_2$ can be calculated using the bond valence sum (BVS) formalism in which each bond with a distance d_{ij} contributes a valence $v_{ij} = \exp[(R_{ij} - d_{ij})/0.37]$ with R_{ij} as an empir-

TABLE I. Crystallographic Data for BaFe₂OSe₂.

Chemical Formula	BaFe ₂ OSe ₂
Formula Mass (g/mol)	422.94
Crystal System	orthorhombic
Space Group	Pmmn (No. 59)
a (Å)	9.8518(7)
b (Å)	4.1332(3)
c (Å)	6.7188(4)
V (Å ³)	273.59(3)
Z	2
Density (g/cm ³)	5.134
$R1/wR2$ ($F_0 > 4\sigma F_0$)/ $R1$ (all data) ^a	0.0459/0.1423/0.0476
Goodness-of-Fit	1.187

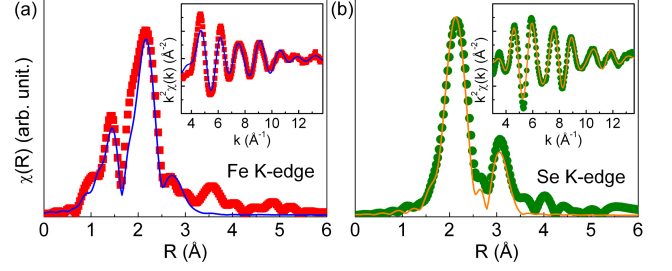
$$^a R1 = \sum |F_0| - |F_c| / \sum |F_0|,$$

$$wR2 = [\sum (|F_0|^2 - |F_c|^2)^2 / \sum (wF_0^2)^2]^{1/2}.$$

FIG. 2. Mössbauer spectrum of BaFe₂OSe₂ at T = 294 K. Inset shows local coordination of Fe atoms in tetrahedra: central smallest ball denote Fe, medium size ball shows oxygen whereas largest balls show selenium atoms.

ical parameter and the total of valences of atom i , V_i equals $V_i = \sum_j v_{ij}$.^{24,25} The calculated valence of Fe ions is +2.23, slightly larger than the apparent oxidation state (+2) for Fe ions. Structural refinement of powder XRD results confirms that all reflections can be indexed in the Pmmn space group and the refined lattice parameters are $a = 9.862(1)$ Å, $b = 4.138(1)$ Å, and $c = 6.732(1)$ Å, close to the values obtained from single crystal XRD. Only (00l) reflections were observed in the single crystal XRD patterns of a BaFe₂OSe₂ (Fig. 1(c)), indicating that the crystallographic c axis is perpendicular to the plane of the single crystal.

Mössbauer fit of BaFe₂OSe₂ consists of two doublets corresponding to the paramagnetic state (Fig. 2). Based on the goodness of fit (0.9995) long range magnetic order is unlikely at 294 K. The first doublet dominates the

FIG. 3. FT magnitudes of the EXAFS oscillations (symbols) for Fe K-edge (a) and Se K-edge (b). The model fits are shown as solid lines. The FTs are not corrected for the phase shifts and represent raw experimental data. Insets of (a) and (b) filtered EXAFS (symbols) with k -space model fits (solid line).

signal and takes 92 % of the fit area with isomer shift of 0.690(1) mm/s. First coordination sphere of Fe (inset of Fig. 2) is tetrahedral with three selenium and one oxygen atoms. Fe²⁺ and Fe³⁺ in FeO₄ tetrahedra have isomer shift values (0.85-0.95) mm/s and (0.2-0.3) mm/s respectively. Isomer shift drops with the increase of effective charge near ⁵⁷Fe. Smaller value of isomer shift in BaFe₂OSe₂ when compared to FeO₄ tetrahedra is consistent with larger covalency of Fe-Se bonds. Isomer shift is in agreement with the calculate value for Fe valence by BVS formalism. Quadrupole shift of 1.594(2) mm/s points to large distortion of tetrahedra. Second doublet has isomer shift of 0.51(1) mm/s and 0.76(3) quadrupole splitting. These parameters are similar to what was observed in other Fe compounds (FeSe₂ or α -FeSe), pointing either to presence of impurities or to intrinsic property of Fe environment in BaFe₂OSe₂. Assuming similar recoil-free factors 8 % of fit area corresponds to approximately similar volume (crystallographic) phase fraction. Since such large impurity fraction would have been detected in our X-ray experiments this might suggest that second doublet comes from undistorted FeSe₄ tetrahedra in BaFe₂OSe₂ with no oxygen bonds present. In other words, there might be 8% ionic disorder existing.

The local environments of Fe and Se such as bond distances are also analyzed by fitting the EXAFS data as show in Fig. 3. For the Fe site, the nearest neighbors are one oxygen atom ($d_{Fe-O} = 1.8769(19)$ Å) and three Se atoms (1×Se(I) and 2×Se(II)) with two different distances ($d_{Fe-Se(I)} = 2.4706(6)$ Å and $d_{Fe-Se(II)} = 2.5540(4)$ Å). The next nearest neighbors are three Fe atoms (1×Fe(I) and 2×Fe(II)) with two different distances ($d_{Fe-Fe(I)} \sim 3.13$ Å and $d_{Fe-Fe(II)} \sim 3.24$ Å). On the other hand, for the Se site, the nearest neighbors are three Fe atoms with bond distances $d_{Fe-Se(I)}$ and $d_{Fe-Se(II)}$. The next nearest neighbors are three Ba atoms (2×Ba(I) and 1×Ba(II)) with two different distances ($d_{Se-Ba(I)} = 3.3541(3)$ Å and $d_{Se-Ba(II)} = 3.4008(4)$ Å). From the joint analysis of Fe and Se edges EXAFS data using a single bond distance for Fe-O, Fe-

TABLE II. Atomic Coordinates, Equivalent Isotropic Displacement Parameters, and Selected Bond Lengths and Angles for BaFe₂OSe₂.

Atom	Wyckoff	x	y	z	U_{eq} (Å ²)
Ba	2b	3/4	1/4	0.49047(4)	0.00734(9)
Fe	4f	0.58580(5)	3/4	0.87890(7)	0.00915(11)
O	2a	3/4	3/4	0.7372(6)	0.0089(5)
Se	4f	0.45734(4)	1/4	0.75887(5)	0.00739(10)
Interatomic Distances (Å)					
Fe-Se	2.4706(6)	Fe-Se	2.5540(4)	Fe-O	1.8769(19)
Ba-Se	3.3541(3)	Ba-Se	3.4008(4)	Ba-O	2.649(2)
Ba-Fe	3.7012(4)				
Bond Angles (°)					
Se-Fe-Se	103.050(15)	Se-Fe-Se	108.03(2)	Se-Fe-O	130.38(10)
Se-Fe-O	105.48(5)	Fe-Se-Fe	76.950(15)	Fe-Se-Fe	108.03(2)
Fe-O-Fe	119.1(2)				

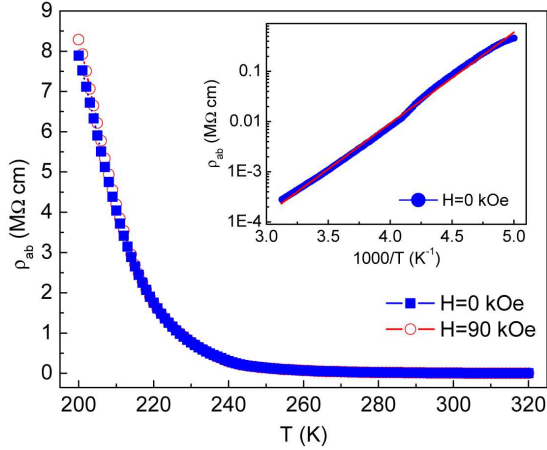


FIG. 4. Temperature dependence of the resistivity $\rho_{ab}(T)$ of the BaFe₂OSe₂ crystal with $H = 0$ (closed blue square) and 90 kOe (open red circle, $H \parallel c$). Inset shows the fitting result of $\rho_{ab}(T)$ at zero field using thermal activation model. The red line is the fitted curve.

Se, Fe-Fe and Se-Ba, and by fitting the k range 2-14 Å⁻¹ for Fe K -edge and 2-12.9 Å⁻¹ for Se K -edge (insets of Fig. 3(a) and (b)), the fitted average bond lengths are $d_{Fe-O} = 1.87(2)$ Å, $d_{Fe-Se} = 2.500(8)$ Å, $d_{Fe-Fe} = 3.17(4)$ Å and $d_{Se-Ba} = 3.38(2)$ Å, which are consistent with the average bond distances derived from XRD fitting.

As shown in Fig. 4, the resistivity $\rho_{ab}(T)$ of BaFe₂OSe₂ crystal increases rapidly with decreasing temperature, suggesting that this compound is a semiconductor in measured temperature region. The semiconducting behavior of $\rho_{ab}(T)$ can be fitted using the thermal activation model $\rho_{ab}(T) = \rho_0 \exp(E_a/k_B T)$, where ρ_0 is a prefactor, E_a is thermal activated energy and k_B is the Boltzmann's constant (inset in Fig. 4). The obtained

E_a is 0.360(2) eV and the room-temperature resistivity $\rho_{ab}(300K)$ is about 10 kΩ·cm. Both are much larger than in BaFe₂Se₃ (0.178 eV and 17 Ω·cm).²² The E_a is also larger than in La₂O₂Fe₂OSe₂ where Fe has octahedral coordination with 4×Se and 2×O mixed anions.²⁶ The large $\rho_{ab}(300K)$ and E_a could be due to the shorter Fe-O bond in highly distorted structure which localizes electrons and increases the band gap. Since La₂O₂Fe₂OSe₂ is a Mott insulator with narrow 3d electronic bands due to strong correlation effects, it is of interest to study whether BaFe₂OSe₂ is normal band insulator or Mott insulator via theoretical calculations. The $\rho_{ab}(T)$ measured at $H = 90$ kOe indicates that there is no obvious magnetoresistance in BaFe₂OSe₂ (Fig. 4).

The Curie-Weiss temperature dependence of $\chi(T)$ is not observed in BaFe₂OSe₂ single crystals up to 350 K (Fig. 5(a)). On the other hand, Mössbauer fit indicate that long range magnetic order is absent at 294 K. It implies that short range magnetic interactions might be present already at the room temperature. There is a peak in the $d(\chi T)/dT$ curve at $T_1 = 240$ K,²⁷ for $H \parallel$ and the values of susceptibility between ZFC and FC curves are nearly the same at this temperature. This peak corresponds to the AFM transition temperature $T_N = 240$ K, confirmed by specific heat measurements. Moreover, the decrease in $\chi_c(T)$ with temperature is more significant than $\chi_{ab}(T)$. It suggests that the easy-axis of magnetization direction could be in ab -plane. According to mean-field theory for collinear antiferromagnets, $\chi(T) \rightarrow 0$ along the easy-axis direction whereas it is nearly constant below T_N for the field perpendicular to the easy-axis direction. With further decreasing temperature, there are two peaks in the $d(\chi T)/dT$ curve at $T_2 = 115$ K and $T_3 = 43$ K, respectively (inset of Fig. 5(a)). The hysteresis between zero-field-cooling (ZFC) and field-cooling (FC) measurements implies that they are spin-glass-like transitions. The absence of hysteresis in isothermal $M(H)$ loops for $H \parallel ab$ (Fig. 4(b)) at $T = 1.8$ K and 250 K indicates that there are no ferromagnetic impurities.

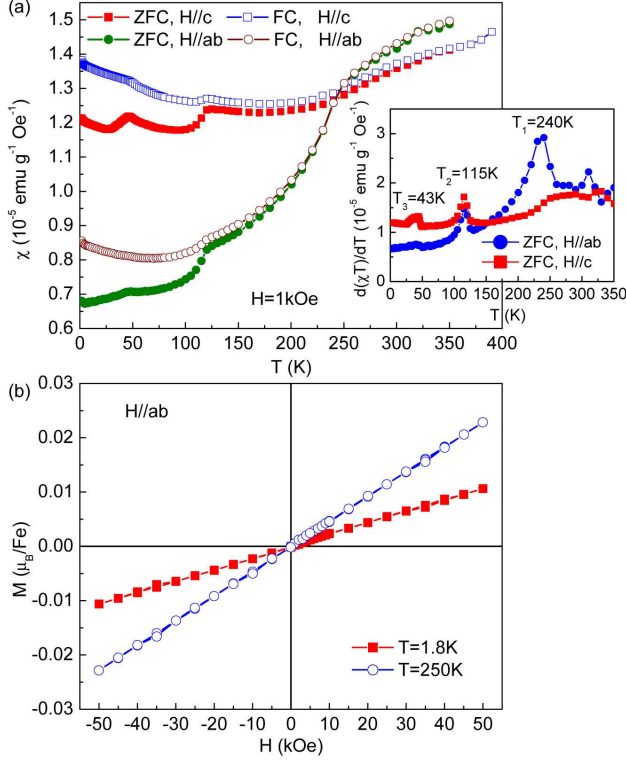


FIG. 5. (a) Temperature dependence of DC magnetic susceptibility $\chi(T)$ under ZFC and FC modes with $H = 1$ kOe along ab-plane and c-axis. (b) Isothermal magnetization hysteresis loops $M(H)$ for $H \parallel ab$ at $T = 1.8$ K and 250 K.

Moreover, the slope of $M(H)$ increases with increasing temperature consistent with the AFM behavior observed in $\chi(T)$ curves (Fig. 5(b)).

As shown in Fig. 6, the specific heat C_p of $\text{BaFe}_2\text{OSe}_2$ approaches the value of $3NR$ at high temperature ($T = 300$ K) assuming $N = 6$, where N is the atomic number in the chemical formula and R is the gas constant ($R = 8.314 \text{ J mol}^{-1} \text{ K}^{-1}$). It confirms the atomic numbers of $\text{BaFe}_2\text{OSe}_2$ obtained from single crystal XRD fitting and consistent with the atomic ratio measured from EDX. On the other hand, at the low temperature, $C_p(T)$ curve can be fitted by a cubic term βT^3 (inset of Fig. 6) and the fitted value β is $0.852(2) \text{ mJ mol}^{-1} \text{ K}^{-4}$. According to the formula $\Theta_D = (12\pi^4 NR/5\beta)^{1/3}$, Debye temperature is estimated to be $\Theta_D = 239.1(2) \text{ K}$. The larger Θ_D when compared to BaFe_2Se_3 ($\Theta_D = 205(1) \text{ K}$) can be ascribed to the smaller atomic mass of oxygen than selenium.²²

There is a λ -type anomaly at $T_1 = 241.7 \text{ K}$ as shown in Fig. 6. The peak position is very close to the peak position ($T_1 = 240 \text{ K}$) at $d\chi(T)/dT$ curve (inset of Fig. 5(a)). It suggests that a long-range AFM ordering forms at this temperature. After subtraction the phonon contribution (C_{ph}) fitted using a polynomial for the total specific heat, the magnetic contribution (C_{mag}) can be obtained. The magnetic entropy can be calculated using the integral

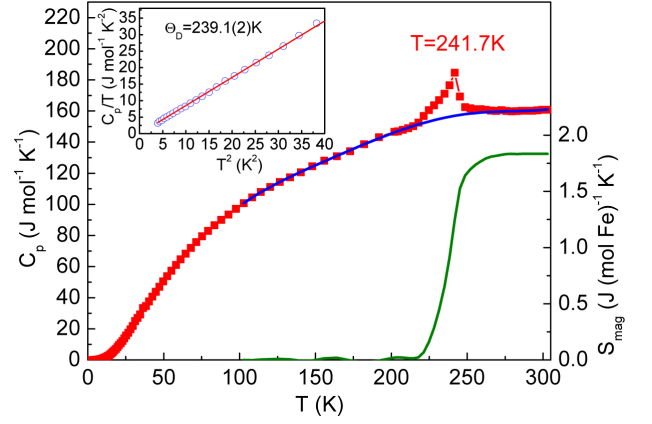


FIG. 6. Temperature dependence of specific heat for $\text{BaFe}_2\text{OSe}_2$ crystal. The horizontal orange line represents the classical value according to Dulong-Petit law at high temperature with $N = 6$. The blue curve represents the phonon contribution fitted by a polynomial. The right axis and its associated green solid curve denote the magnetic entropy. Inset: the low-temperature specific-heat data in the plot of C_p/T vs T^2 . The red solid line is the fitting curves using formula $C_p/T = \beta T^2$.

$S_{mag}(T) = \int_0^T C_{mag}/T dt$. The derived S_{mag} is $\sim 1.83 \text{ J/mol-K}$ when T is up to 300 K (Fig. 6), which is much smaller than expected values $R \ln(2S + 1)$ for Fe^{2+} ions with low spin state ($\sim 20\% R \ln 3$) and with high spin state ($\sim 13.7\% R \ln 5$) in tetrahedral crystal fields. It is even less than $R \ln 2$ for $S = 1/2$ ($\sim 31.8\% R \ln 2$), suggesting that there is short range magnetic order at higher temperature which partially releases the magnetic entropy before any long range magnetic transition, consistent with the Mössbauer spectrum and magnetization measurement results. On the other hand, there is no peaks appear at $T_3 = 115 \text{ K}$ and $T_4 = 43 \text{ K}$, confirming the glassy magnetic behaviors at those temperatures.

IV. CONCLUSION

In summary, we report a discovery of a new layered iron oxychalcogenide $\text{BaFe}_2\text{OSe}_2$. The crystal structure features double chains of edge-shared Fe-Se(O) tetrahedra that propagate along the b -axis. The Fe-Se(O) double chains are bridged by oxygen along the a -axis. $\text{BaFe}_2\text{OSe}_2$ single crystals are magnetic semiconductors with a possible long range AFM transition at 240 K and two glassy transitions at 115 K and 43 K. The magnetic entropy up to 300 K is much smaller than expected for Fe^{2+} in tetrahedral crystal fields, suggesting the existence of short range AFM correlation above room temperature. Because of the interesting structure and connectivity among the iron atoms, it is of interest to investigate the mechanism of magnetic ground state by theoretical calculations and by neutron scattering experiments. Moreover, doping effects on physical properties should further reveal similarities and differences with supercon-

ducting iron selenide compounds.

V. ACKNOWLEDGEMENTS

We thank Kefeng Wang for helpful discussion, and Syed Khalid for help with XAFS measurements. Work

at Brookhaven is supported by the U.S. DOE under Contract No. DE-AC02-98CH10886 A.I.F. acknowledges support by U.S. Department of Energy Grant DE-FG02-03ER15476. Beamline X19A at the NSLS is supported in part by the U.S. Department of Energy Grant No DE-FG02-05ER15688. This work has also been supported by the grant No. 171001 from the Serbian Ministry of Education and Science.

-
- ¹ Y. Kamihara, T. Watanabe, M. Hirano, and H. Hosono, *J. Am. Chem. Soc.* **130**, 3296 (2008).
 - ² S. J. Clarke, P. Adamson, S. J. C. Herkelrath, O. J. Rutt, D. R. Parker, M. J. Pitcher, and C. F. Smura, *Inorg. Chem.* **47**, 8473 (2008).
 - ³ S. Adachi, T. Tatsuki, T. Tamura, and K. Tanabe, *Chem. Mater.* **10**, 2860 (1998).
 - ⁴ K. Ueda, S. Inoue, S. Hirose, H. Kawazoe, and H. Hosono, *Appl. Phys. Lett.* **77**, 2701 (2000).
 - ⁵ H. Hiramatsu, K. Ueda, H. Ohta, M. Hirano, T. Kamiya, and H. Hosono, *Appl. Phys. Lett.* **82**, 1048 (2003).
 - ⁶ H. Kamioka, H. Hiramatsu, H. Ohta, M. Hirano, K. Ueda, T. Kamiya, and H. Hosono, *Appl. Phys. Lett.* **84**, 879 (2004).
 - ⁷ J. M. Mayer, L. F. Schneemeyer, T. Siegrist, J. V. Waszczak, and B. v. Dover, *Angew. Chem., Int. Ed. Engl.* **31**, 1645 (1992).
 - ⁸ C. Wang, M.-Q. Tan, C.-M. Feng, Z.-F. Ma, S. Jiang, Z.-A. Xu, G.-H. Cao, K. Matsubayashi, and Y. Uwatoko, *J. Am. Chem. Soc.* **132**, 7069 (2010).
 - ⁹ N. Ni, E. Climent-Pascual, S. Jia, Q. Huang, and R. J. Cava, *Phys. Rev. B* **82**, 214419 (2010).
 - ¹⁰ F. Han, X. Y. Zhu, G. Mu, P. Cheng, and H.-H. Wen, *Phys. Rev. B* **78**, 180503 (2008).
 - ¹¹ H. Kabbour, E. Janod, B. Corraze, M. Danot, C. Lee, M.-H. Whangbo, and L. Cario, *J. Am. Chem. Soc.* **130**, 8261 (2008).
 - ¹² R. H. Liu, J. S. Zhang, P. Cheng, X. G. Luo, J. J. Ying, Y. J. Yan, M. Zhang, A. F. Wang, Z. J. Xiang, G. J. Ye, and X. H. Chen, *Phys. Rev. B* **83**, 174450 (2011).
 - ¹³ X. C. Wang, Q. Q. Liu, Y. X. Lv, W. B. Gao, L. X. Yang, R. C. Yu, F. Y. Li, and C. Q. Jin, *Solid State Commun.* **148**, 538 (2008).
 - ¹⁴ D. R. Parker, M. J. Pitcher, P. J. Baker, I. Franke, T. Lancaster, S. J. Blundell, and S. J. Clarke, *Chem. Commun.* **16**, 2189 (2009).
 - ¹⁵ J. B. He, D. M. Wang, H. L. Shi, H. X. Yang, J. Q. Li, and G. F. Chen, *arxiv*: 1104.2176 (2011).
 - ¹⁶ APEX2 Ver. 2008.5; Bruker AXS, Inc.: Madison, WI (2008).
 - ¹⁷ G. M. Sheldrick, *Acta Crystallogr.* **A64**, 112 (2008).
 - ¹⁸ Hunter B. (1998) "Rietica - A visual Rietveld program", International Union of Crystallography Commission on Powder Diffraction Newsletter No. 20, (Summer) <http://www.rietica.org>
 - ¹⁹ R. Prins and D. Koningsberger, *X-ray Absorption: Principles, Applications, Techniques of EXAFS, SEXAFS, XANES*, Wiley, New York (1988).
 - ²⁰ R. A. Brand, WinNormos Mössbauer fitting program, Universität Duisburg 2008
 - ²¹ J. Guo, S. Jin, G. Wang, S. Wang, K. Zhu, T. Zhou, M. He, and X. Chen, *Phys. Rev. B* **82**, 180520(R) (2010).
 - ²² H. C. Lei, H. J. Ryu, A. I. Frenkel, and C. Petrovic, *Phys. Rev. B* **84**, 214511 (2011).
 - ²³ H. C. Lei, M. Abeykoon, E. S. Bozin, K. F. Wang, J. B. Warren, and C. Petrovic, *Phys. Rev. Lett.* **107**, 137002 (2011).
 - ²⁴ I. D. Brown, and D. Altermatt, *Acta Crystallogr. Sect. B* **41**, 244 (1985).
 - ²⁵ N. E. Brese, and M. O'Keeffe, *Acta Crystallogr. Sect. B* **47**, 192 (1991).
 - ²⁶ J.-X. Zhu, R. Yu, H. D. Wang, L. L. Zhao, M. D. Jones, J. H. Dai, E. Abrahams, E. Morosan, M. H. Fang, and Q. M. Si, *Phys. Rev. Lett.* **104**, 216405 (2010).
 - ²⁷ M. E. Fisher, *Philos. Mag.* **7**, 1731 (1962).